

Interaction between a flexible filament and a downstream rigid body

Fang-Bao Tian,^{1,2} Haoxiang Luo,² Luoding Zhu,³ and Xi-Yun Lu¹

¹*Department of Modern Mechanics, University of Science and Technology of China, Hefei, Anhui 230026, China*

²*Department of Mechanical Engineering, Vanderbilt University, 2301 Vanderbilt Place, Nashville, Tennessee 37235-1592, USA*

³*Department of Mathematical Sciences, Indiana University–Purdue University Indianapolis, 402 North Blackford Street, Indianapolis, Indiana 46202, USA*

(Received 11 February 2010; published 3 August 2010)

A filament flapping in the bow wake of a rigid body is considered in order to study the hydrodynamic interaction between flexible and rigid bodies in tandem arrangement. Both numerical and experimental methods are adopted to analyze the motion of the filament, and the drag force on both bodies is computed. It is shown that the results largely depend on the gap between the two objects and the Reynolds number. The flexible body may have larger vibration amplitude but meanwhile experience a reduced drag force. On the other hand, the trailing rigid body enjoys a drag reduction. The qualitative behavior of the filament is independent of the filament's length and mass ratio or the shape of the rigid body for the parameter regime considered. The result is in contrast with the interaction between two rigid or two flexible objects in tandem arrangement, and it may provide a physical insight into the understanding of the aquatic animals swimming in the bow wake of ships or staying in the bow wake of stationary structures.

DOI: [10.1103/PhysRevE.82.026301](https://doi.org/10.1103/PhysRevE.82.026301)

PACS number(s): 47.63.mf, 47.15.Tr

I. INTRODUCTION

The hydrodynamic interaction of multibodies immersed in a fluid is common in daily life. Aircrafts flying and ships cruising in formation are well-known examples of the interaction between rigid objects. In the situation that one rigid object is located in the downstream wake of another, the trailing object enjoys a drag decrease [1,2]. This phenomenon can be easily explained by the conventional theory of hydrodynamic drafting. Recently, numerical and experimental methods have been adopted to study the interaction between flexible bodies [3–5]. In the configuration of two flexible slender bodies in tandem arrangement, the downstream one suffers a drag increase and flaps with a larger amplitude [4,5], which is in contrast with the interaction between rigid bodies. Given the drastic difference between the rigid-rigid and flexible-flexible systems, it would be interesting to examine the situation where the system consists of both rigid and flexible bodies and the bodies are within the distance of hydrodynamic interaction. The examples of such an interaction in real life include fish swimming in the downstream or bow wake of solid structures and dolphins riding in the bow wake of ships [6–11]. In the case that the flexible body is located in the downstream wake of a rigid body such as a cylinder, experiments and numerical simulations have shown that the flexible bodies can gain considerable thrust [12–14]. In comparison, it is still not clear what would happen if the flexible body is located on the upstream side of the rigid body. Liao *et al.* [6] found that a fish swimming in the bow wake of a bluff body uses less amount of energy than a fish swimming in an otherwise free environment. Since the fluid immediately upstream of the bluff body is being “pushed” while the fluid downstream is being “dragged,” it is expected that the fish could take advantage of the bow wake for drag reduction in the same way as the draft effect in the rear wake. However, since the fish body is essentially flexible and undergoes an undulating motion, we speculate that additional

mechanism of hydrodynamic interaction could exist between the two bodies.

In order to investigate the issue, we apply a two-dimensional numerical simulation and also an experimental technique to study the behavior of a flexible filament passively vibrating in the bow wake of a rigid cylinder or a flat plate of finite length.

II. PHYSICAL PROBLEM AND MATHEMATICAL FORMULATION

As shown in Fig. 1, a thin filament with length L is placed in upstream of a cylinder with diameter d . The minimum distance between the filament and the cylinder is G . The fluid density and viscosity are ρ and μ , respectively, and the free-stream velocity is U . The surrounding fluid is governed by the two-dimensional incompressible Navier-Stokes equation and the continuity equation,

$$\rho \frac{D\mathbf{u}}{Dt} = -\nabla p + \mu \nabla^2 \mathbf{u} + \mathbf{b}, \quad \nabla \cdot \mathbf{u} = 0, \quad (1)$$

where $\mathbf{u}=(u,v)$ is the fluid velocity, p is the pressure, \mathbf{b} is the body force, and D/Dt is the material derivative.

We assume that the filament has a large stretching coefficient and is thus nearly inextensible. The governing equation for dynamics of the filament in the two-dimensional plane is [15]

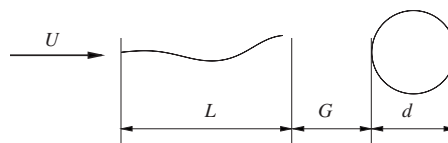


FIG. 1. A schematic of the filament-cylinder system.

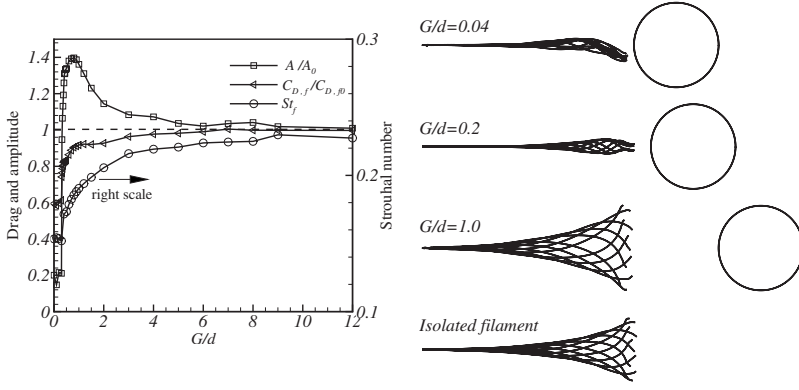


FIG. 2. The simulation results for $Re=100$, $S=0.3$, and $L/d=2.5$. (a) The drag ratio $C_{D,f}/C_{D,f0}$, amplitude ratio A/A_0 , and Strouhal number of the filament as functions of G/d ($A_0/d=0.75$ in this case). (b) Typical flapping modes of the filament.

$$m_s \frac{\partial^2 \mathbf{X}}{\partial t^2} - \frac{\partial}{\partial s} \left[T(s) \frac{\partial \mathbf{X}}{\partial s} \right] + K_b \frac{\partial^4 \mathbf{X}}{\partial s^4} = \mathbf{F}, \quad (2)$$

where m_s is the linear density, \mathbf{X} is the position vector of a point on the filament, s is the arclength along the filament, $T(s)=K_s(|\frac{\partial \mathbf{X}}{\partial s}|-1)$ is the in-plane tension, and \mathbf{F} is the hydrodynamic traction per unit length. Here, K_s and K_b are the stretching and bending coefficients of the filament, respectively. The traction is given by $\mathbf{F}=[(-p\mathbf{I}+2\mathbf{E})^+ - (-p\mathbf{I}+2\mathbf{E})^-] \cdot \mathbf{n}$, where \mathbf{E} is the shear stress tensor, \mathbf{I} is the identity matrix, “+” and “-” denote the two sides of the filament, and \mathbf{n} is the normal vector pointing to the + side. The leading point of the filament is hinged, and the trailing point is free. Therefore, the bending moment vanishes at the head and tail, and the shear stress at the tail is zero. The corresponding boundary conditions are thus $\mathbf{X}|_{s=0}=\mathbf{X}_0$, $(\partial^2 \mathbf{X}/\partial s^2)|_{s=0}=0$, $(\partial^2 \mathbf{X}/\partial s^2)|_{s=L}=0$, and $(\partial^3 \mathbf{X}/\partial s^3)|_{s=L}=0$. The nondimensional groups governing the system are the Reynolds number $Re=\rho U d/\mu$, mass ratio $S=m_s/(\rho d)$, bending rigidity $E_b=K_b/(\rho U^2 d^3)$, L/d , and G/d .

The fluid-structure interaction is solved at low Reynolds numbers using a modified penalty immersed boundary method (PIBM) coupled with a lattice Boltzmann method (LBM) (see the Appendix for more details about the method and the validation tests). The complementary laboratory experiment at $Re=390$ has been carried out in a vertical flowing soap film tunnel in the same way as described in Refs. [3,14]. The soap film is formed between two parallel nylon wires, and its surface density is $1.5-3 \times 10^{-4}$ g/cm². A cylinder with the diameter of 0.6 cm is inserted perpendicularly into the film. A silk filament with the diameter of 150 μ m, length of 2 cm, linear density of $1.3-2 \times 10^{-4}$ g/cm, and

bending stiffness of 0.62 g cm³/s² is set in the bow wake of the cylinder with its leading edge fastened to a thin wire that extends out of the film. The rest of the filament hangs free in the film. The flow speed of the soap film is 130 cm/s, and the kinematic viscosity is 0.2 cm²/s. The soap film is illuminated by three high-pressure sodium lamps. The motion of the filament is recorded by a high-speed digital video camera (Mikrotron, MC1310) at 2004 frames per second. More details of the setup can be found in Refs. [3,14,16].

III. RESULTS AND DISCUSSION

In this study, we will focus on the influence of Re , G/d , L/d , and S . The rigidity of the filament, E_b , is set to be on order of 10^{-4} . At this level, the filament vibration is no longer sensitive to E_b [15]. The normalized stretching coefficient $K_s/(\rho U^2 d)$ is $O(10^3)$ to make sure the filament extension is small and the simulation is stable. In all simulations, we introduce a small-amplitude sinusoidal perturbation to the initial state of the filament, while keeping the filament length unchanged, to induce the onset of instability.

A. Effect of Re and G/d

First, we consider the effect of G/d on the filament behavior at $Re=100$, $S=0.3$, and $L/d=2.5$. Figure 2(a) shows the amplitude ratio A/A_0 and the drag ratio $C_{D,f}/C_{D,f0}$ for a range of filament-cylinder gap widths. Here, A is the vibration amplitude of the tail of the filament and $C_{D,f}$ is the drag coefficient of the filament defined as the total drag normalized by $\frac{1}{2}\rho U^2 d$. A_0 and $C_{D,f0}$ are the amplitude and drag coefficient of the corresponding filament in the absence of the cylinder. When $G/d < G_c^*=0.33$, the motion of the fila-

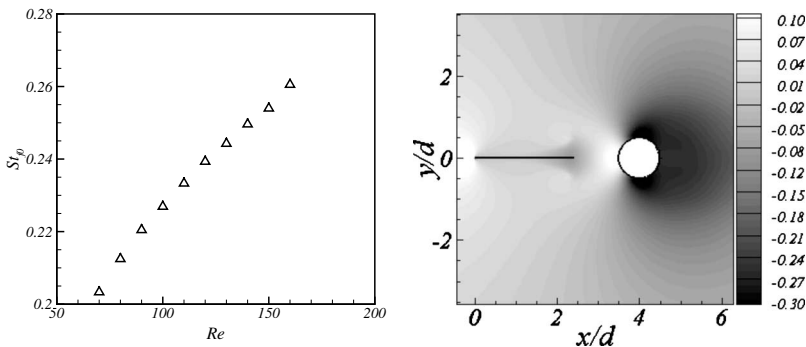


FIG. 3. (a) The Re - St_{f0} relationship of a lone filament with $S=0.3$ and $L/d=2.5$. (b) The time-average pressure field for $Re=100$, $S=0.3$, $L/d=2.5$, and $G/d=1.0$, where the bright color represents a high value.

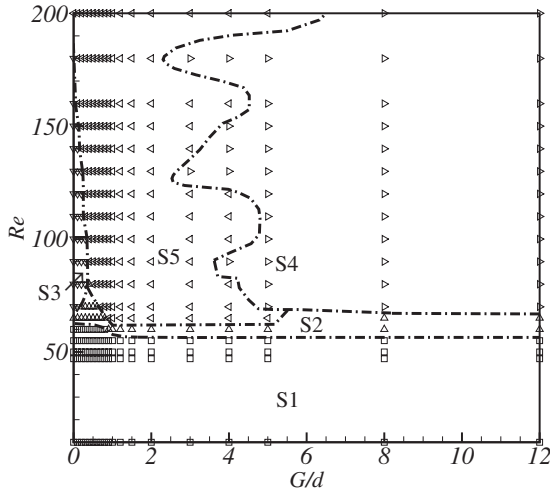


FIG. 4. The state diagram on the Re - G/d plane for $S=0.3$ and $L/d=2.5$. S1–S5 represent, respectively, the stable state, vortex shedding state, suppressed state, disassociated state, and amplified state.

ment is suppressed, and the flapping amplitude is smaller than that of the isolated filament. Apparently, the suppressed vibration is due to the viscous shear in the small filament-cylinder gap, caused by the tail oscillation. An inhibited behavior similar to the present case was also observed for the filament flapping upstream of another filament with close separation [4,5]. When G/d is larger than G_c^* , the vibration amplitude increases sharply, and the filament jumps from a suppressed state to an amplified state, where A/A_0 becomes significantly higher than unity. The vibration arrives at its peak when $G/d=0.8$, where the amplitude is 40% higher than that of the corresponding isolated filament. As G/d is increased further, the filament amplitude decreases and, as expected, approaches to that of the isolated filament due to the diminishing interaction. When $G/d > 5.0$, the difference between A and A_0 is within 5%. The vibration pattern of the filament is shown in Fig. 2(b) for $G/d=0.04, 0.2, 1.0$, and ∞ (isolated filament). Note that the mean position of the filament for $G/d=0.04$ is skewed. This phenomenon will be discussed later. For $G/d=1.0$, the amplitude grows as the deformation wave travels from the filament head to the tail, resembling a flapping flag in the wind [17]. Surprisingly, despite the amplitude overshoot in Fig. 2(a), the drag on the filament is always lower than that of the corresponding isolated filament. As shown in Fig. 2(a), the ratio $C_{D,f}/C_{D,f_0}$ increases almost monotonically from around 0.2 and later gradually approaches to unity when G/d is raised from zero to 12.

The interesting interaction between the filament and cylinder observed here is different from that of rigid-rigid or of flexible-flexible bodies, and therefore requires a new expla-

nation. For this purpose, we first define the Strouhal number for the filament, $St_f=f_f d/U$, and the Strouhal number for the cylinder, $St_c=f_c d/U$, where f_f is the flapping frequency and f_c is the frequency of vortex shedding behind the cylinder. At $Re=100$, the Strouhal number for the corresponding isolated filament is 0.23 based on our numerical simulation, while for the isolated cylinder, the Strouhal number is much lower, $St_c=0.166$ [18]. Our separated simulations also show that, for a lone filament in the Reynolds number ranging from 50 to 200, St_f decreases as the Reynolds number is reduced [Fig. 3(a)]. When the cylinder is introduced behind the filament, the effective Reynolds number becomes lower for the filament since the flow around the filament is impeded by the cylinder. Therefore, according to the St_f - Re relationship, the filament’s flapping frequency also decreases when the cylinder is present. At a certain gap width, the filament frequency may become close to that of the vortices shed from the cylinder, and a resonance would take place and strengthen the filament’s vibration. In the resonance region, a wake-mediated synchronization and the mixed vortex wake are observed, a phenomenon also reported by Alben [19] in the flexible-flexible system. Further details of the vortex interaction are provided later when we discuss the flow field. The frequency matching is confirmed by the observation in Fig. 2(a) that the Strouhal number of the filament at peak vibration is $St_f=0.186$ at $G/d=0.8$ and is approximately equal to the Strouhal number of vortex shedding from the cylinder, which has been slightly increased compared to the isolated cylinder. Note that the resonance here refers to the vortex-vortex interaction in the flow, and the structural frequencies of the filament (at least first a few modes) are much lower than the system frequency here and are thus not involved.

To explain the counterintuitive drag reduction while the filament’s vibration is amplified during the resonance, we point out that the presence of the cylinder provides an obstructing mechanism, reducing the flow speed and raising the pressure downstream the filament [see the time-averaged pressure field in Fig. 3(b)]—both factors reduce the drag force on the filament.

To study the combined effect of the Reynolds number and the gap width, we have run a series of simulations by systematically varying Re from 10 to 200 and G/d from nearly zero to 12. The length and mass of the filament are $L/d=2.5$ and $S=0.3$, respectively. The simulation results are grouped according to the behavior of flow and filament, as shown by the state diagram in Fig. 4. For the parameter range considered here, there are five states on the Re - G/d map, which are labeled from S1 to S5. The simulations belonging to each state are marked with a unique symbol. It should be pointed out that in the present study, the borderlines between the states are not defined with high accuracy but are approximately drawn based on the parameter spacing in the simulation series. The resolution can be seen from the

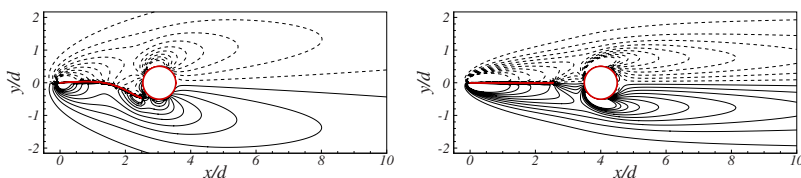


FIG. 5. (Color online) State S1: the steady vorticity contours for $Re=10$, $G/d=(a)$ 0.04 and (b) 1.0. The negative-valued contours are shown as broken lines.

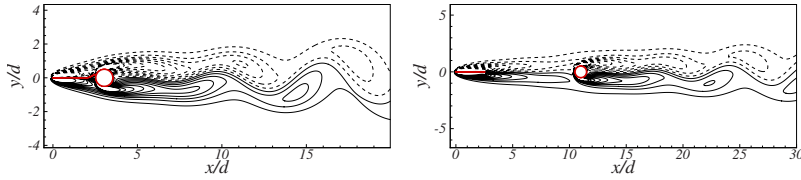


FIG. 6. (Color online) State S2: instantaneous vorticity contours for $Re=65$, $G/d=(a)$ 0.04 and (b) 8.0.

distribution of the data points on the state map. Next, we describe the characteristic system behavior within each state regime.

In state S1 where Re is less than 55, the filament is stable, and there is no vortex shedding behind the cylinder. Note that for a lone cylinder, vortex shedding takes place when $Re > 47$ [20]. In the present case, the threshold Reynolds number is increased because the filament slows down the upstream flow and provides a stabilizing mechanism. The typical flow field at this state is shown in Fig. 5 where $Re = 10$ and $G/d = 0.04$ and 1.0. When G/d is small, the tail of the filament is deflected by the flow stream, settling down on either side of the cylinder. Which side the filament takes depends on the sign of the initial perturbation of the filament. The amplitude of deflection is $0.46d$ for $G/d = 0.04$, and it decreases as the filament-cylinder gap is increased. For $G/d = 1.0$, the filament settles down to the midplane, and the system becomes symmetric. The result suggests that at such Reynolds numbers, a critical gap width exists at which the system bifurcates. When G/d is smaller than the critical value, the symmetrical configuration is no longer stable, and the system would take one of the asymmetric equilibrium configurations.

As Re is increased, the system enters state S2, which is mainly in a banded region roughly between $Re = 55$ and 70 (Fig. 4). Within this state, the filament remains stationary, but vortices start to shed from the cylinder. The typical flow field at this state is shown in Fig. 6 where $Re = 65$ and $G/d = 0.4$ and 8.0. The filament behavior is similar to that in state S1. That is, for small G/d , the filament takes side but remains stable [Fig. 6(a)], and for large G/d the filament stays on the symmetry line [Fig. 6(b)]. For $G/d = 0.04$, the deflection amplitude is $0.19d$, which is smaller compared to that for $Re = 10$ shown in Fig. 5(a).

As the Reynolds number is further raised above 80, the situation becomes more complex, and the flow exhibits three behaviors, namely, the suppressed state (S3), disassociated state (S4), and amplified state (S5). In the suppressed state S3, where G/d is small (Fig. 4), the flapping motion of the filament is inhibited by the lateral flow in the filament-cylinder gap, and the filament has a reduced vibration amplitude compared to the corresponding isolated filament. The flow field at this state is shown in Fig. 7 where $Re = 100$ and $G/d = 0.04$ and 0.2. For $G/d = 0.04$, the filament vibrates lo-

cally on one side of the cylinder and never crosses the midplane to reach the other side, while for $G/d = 0.2$ the filament vibrates around the midplane in the form of a traveling wave. Note that the definition of A in this state involves only the oscillatory component, and the steady component is excluded. For $G/d = 0.04$, the averaged deflection of the tail is $0.17d$.

In the dissociated state S4, where G/d is larger than 5 (Fig. 4), the filament is independent of the cylinder and behaves like a lone filament. A typical flow field in this state is shown in Fig. 8 where $Re = 100$ and $G/d = 8.0$. It can be seen that the vortices shed from the filament impinge on the cylinder and still interact with the vortices generated from the cylinder surface. However, the interaction is too weak to cause any significant effect on the filament.

Between the suppressed and dissociated states, there is the amplified state, where the resonance takes place and vibration of the filament is enhanced, i.e., A/A_0 larger than unity. A typical flow field in this state is shown in Fig. 9 where $Re = 100$ and $G/d = 1.0$. As discussed earlier, the vortex shedding frequency of the filament matches that of the cylinder. The sequence of the flow field shows that the vortices shed from the filament interact with the vortices generated at the cylinder surface in a well-coordinated manner. For example, in Figs. 9(a) and 9(b), a negative vortex is stretched out from the tail end of the filament, and due to the rising motion of the tail this vortex is brought to the top side of the cylinder, where the vortex is also negative. In Fig. 9(c), the negative vortex from the filament breaks off and merges into the vortex attached to the cylinder. Meanwhile, another negative vortex downstream the cylinder is breaking off from the newly merged vortex. Finally, the merged vortex starts to detach from the cylinder [Fig. 9(d)], preparing for next shedding event. Similarly, the coordinated shedding and merging of the positive vortices take place on the other side of the cylinder.

We should point out that the resonant flapping here is unlikely a process of the filament oscillating between the two asymmetric equilibrium configurations that may exist as in states S1 and S2 where Re is low. As shown in Figs. 5–7, the steady deformation of the filament decreases as Re is increased, and the amplitude of the steady component is less than $0.2d$ when the filament starts to vibrate. For moderate gap widths, $G/d \sim 1$, the steady component is zero. On the

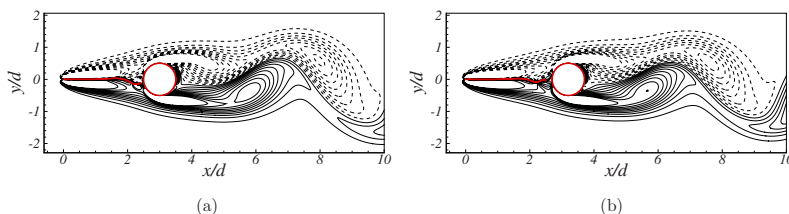


FIG. 7. (Color online) State S3: instantaneous vorticity contours for $Re = 100$, (a) $G/d = 0.04$ and (b) $G/d = 0.2$.

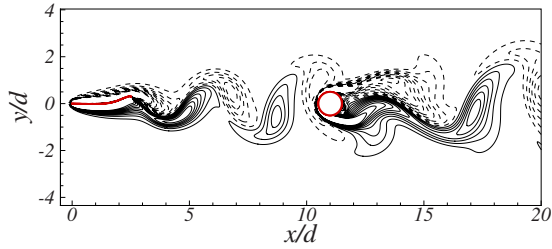


FIG. 8. (Color online) State S4: instantaneous vorticity contours for $Re=100$ and $G/d=8.0$.

other hand, the resonant flapping has an amplitude approximately equal to or even larger than d in the present simulations.

When the Reynolds number is above 180, the suppressed state disappears on the state diagram. This is because as Re is increased, the viscous effect in the gap is reduced and meanwhile the destabilizing effect due to the fluid inertia becomes stronger. The amplitude and drag ratios of such a case are plotted in Figs. 10(a) and 10(b) for $Re=200$, $L/d=2.5$, and $S=0.3$, where A/A_0 is above unity ($A_0/d=0.85$ based on our simulation) but $C_{D,f}/C_{D,f_0}$ is still less than unity. The effect of the Reynolds number on the vibration amplitude and drag coefficient is more clearly seen by plotting the data along a vertical line with fixed G/d in the state diagram. The result is shown in Fig. 11 for $G/d=1.0$. Note that the amplitude and drag of the isolated filament depend on the Reynolds number and therefore are not used here for normalization. Three states S1, S2, and S5 are involved in this figure. For $Re < 60$, the system belongs to state S1 or S2, where the filament is stable (and remains in the midplane for this gap ratio) and $A/d=0$. Beyond $Re=60$, the system undergoes a sharp transition, and the filament starts to flap with a large amplitude. The amplitude further increases as Re is increased, and it then reaches a constant around $A/d=1.0$ when Re is larger than 110. Despite of the increasing flapping amplitude, the drag coefficient displays an overall decreasing trend, which is consistent to the drag reduction phenomenon at the resonance state.

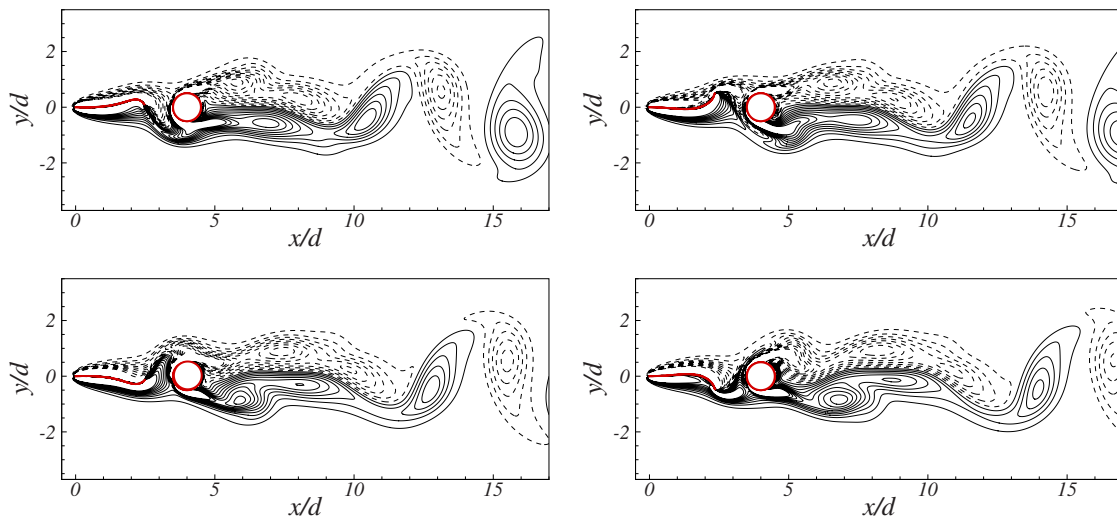


FIG. 9. (Color online) State S5: instantaneous vorticity contours for $Re=100$ and $G/d=1.0$ where the time interval between the frames is $1.1d/U$ (see the supplementary material [21] for an animation).

Note that the borders between the states on the state map in Fig. 4 are somewhat ragged, reflecting the complexity of the system. For example, part of state S1 intrudes upon state S2 at low G/d , which is understandable because the stabilizing effect of the filament on the flow around the cylinder is stronger when the gap is smaller. The irregularity of the state borders is less intuitive in other cases.

The existence of the amplified state in the present filament-cylinder system is confirmed by the experiments performed in the soap film. The amplitude ratio A/A_0 from the experimental tests is shown in Fig. 10(a) for $Re=390$ and $L/d=3.3$, where A/A_0 gradually decreases from 2.5 and approaches unity as G/d varies from zero to 8. The experiment in the absence of the cylinder shows that the vibration amplitude of the filament is $0.75d$. Figure 12 shows the images obtained by the high-speed camera for $G/d=1.0$. It can be seen that the vibration pattern of the filament is similar to that shown in Fig. 9 from the numerical simulation.

Based on the parameters given in Sec. II, the equivalent mass ratio in the experiment is between 0.72 and 2.22, and the dimensionless bending rigidity is 0.57–1.13. Unfortunately, our numerical simulations fail to converge at this condition because the mass ratio and Reynolds number are high. Nevertheless, the numerical simulations presented here are consistent with the experimental observation, for in both cases an amplified flapping state exists during the hydrodynamic interaction of the filament and the cylinder at close range.

B. Effect of L/d and S

The normalized length of the filament, L/d , also plays an important role in the flow-structure interaction. We present the amplitude and drag ratios of three different filament lengths, $L/d=1.0$, 2.5, and 4.0, in Figs. 10(a) and 10(b), where $Re=100$ and $S=0.3$. The vibration amplitude of the corresponding isolated filament is $A_0/d=0.55$, 0.75, and 0.72, for $L/d=1.0$, 2.5, and 4.0, respectively. It can be seen that for these three cases, the filament resonance occurs at

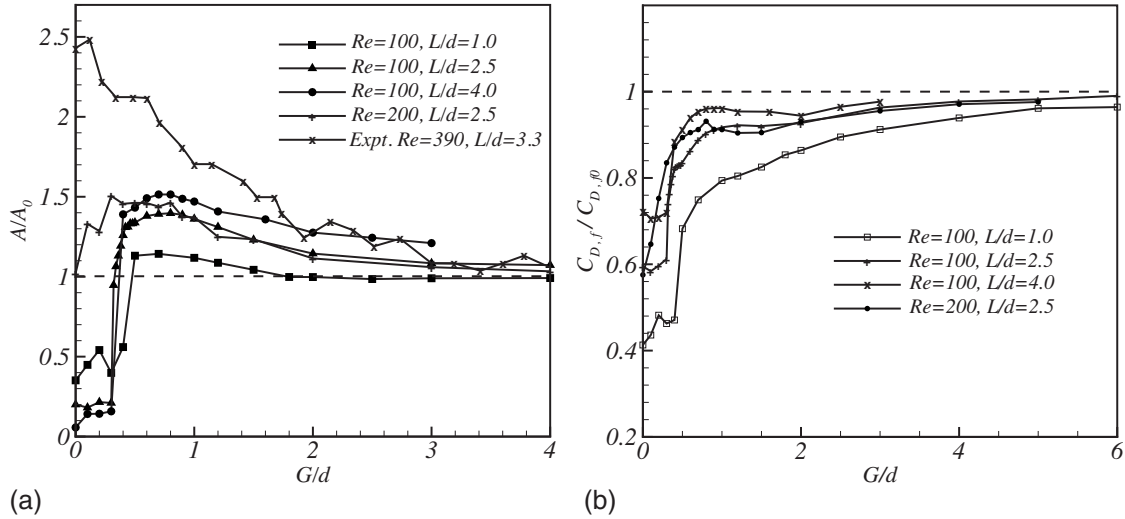


FIG. 10. (a) The amplitude ratio and (b) drag ratio against G/d for $S=0.3$ and several Reynolds numbers and filament lengths. The amplitude ratio for the film flow experiment is shown in (a).

roughly the same critical gap width from $G/d=0.8$ to 1.0 . However, the longer filaments exhibit higher resonant amplitude ratios. For $L/d=4.0$, A/A_0 reaches a peak of 1.51. On the other hand, the drag reduction at resonance is more dramatic for smaller filament length. For $L/d=1.0$, this drag ratio is around 0.8.

It has been shown previously that a single massless filament is stable when immersed in a uniform flow and flapping occurs when the mass ratio exceeds a critical value that depends on the Reynolds number [22,23]. Therefore, the mass of the filament has a destabilizing effect on the system. In our simulation, the critical Reynolds number for an isolated filament of $S=0.3$ to flap is around 70, which is higher than $Re=47$, the critical Reynolds number for the flow past a lone cylinder to become unstable [20]. To investigate the effect of S in the present system, we have performed a series of simulations at $S=0.5$, $Re=40$, and $L/d=2.5$. Note that at this Reynolds number, the flow around a lone cylinder is stable, but the flow past the single filament is unstable and the flapping amplitude is $A_0/d=1.80$. Figure 13(a) shows the amplitude and drag ratios of the filament as functions of G/d . The result reveals that the resonance still occurs at such a low Reynolds number. At resonance where $G/d=1.2-1.5$, the amplitude ratio of the filament reaches around 280%. Therefore, we conclude that the inertia of the filament promotes onset of the resonance. Another interesting observation is that even though the flapping amplitude of the filament at resonance is increased near three times, the drag is only about the same as that of the isolated filament.

C. Effect of the body geometry

To study the effect of the shape of the rigid body downstream of the filament, we replace the cylinder with a thin rigid plate of length d . The numerical simulations reveal that a similar resonant behavior takes place. The amplitude and drag ratios are plotted for this case in Fig. 13(b) for $Re=100$, $S=0.3$, and $L/d=2.5$. A similar resonant state is also

observed when G/d is between 0.5 and 2.0. However, the amplification of the filament flapping at resonance is only up to 115%, which is much lower compared to the corresponding cylinder case. In addition, because the plate is a slender body and raises the average pressure behind the filament only slightly, the drag on the filament in the amplified state is nearly the same as that on the isolated filament. The typical flow field is shown in Fig. 14 for $G/d=1.0$. It can be seen that the vortices shed from the filament merge into the two vortex sheets next to the rigid plate, causing the vortex sheets to detach from the plate and break off periodically. As in the cylinder case, the vortex shedding from the plate is also synchronized with the vortex shedding from the filament. Note that the flow is stable for the isolated rigid plate at this Reynolds number and the vortex sheets would remain continuous. Therefore, the resonance in the coupled filament-plate system is triggered and sustained by the unsteady vortices coming from the filament. Finally, we would like to point out that all cases in our simulation show that the trailing rigid object always enjoys a drag reduction, which is similar to that in the solid-solid bodies in tandem arrangement [1,2].

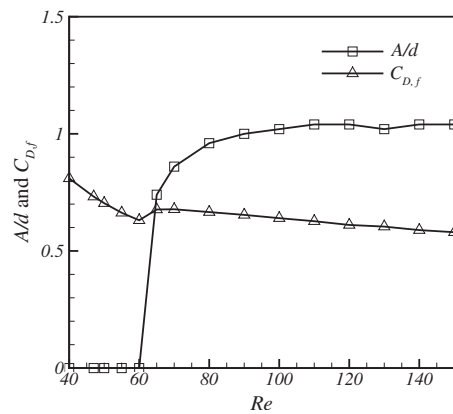


FIG. 11. The amplitude normalized by d and the drag coefficient of the filament at $G/d=1.0$.

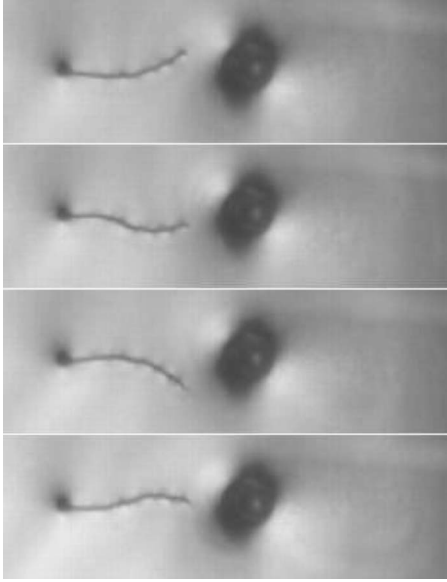


FIG. 12. Images of filament vibration in the presence of a cylinder from the soap film experiment for $G/d=1.0$. The time interval is 9.5 ms. The filament length is 2 cm.

IV. CONCLUDING REMARKS

In summary, our numerical simulations show that there is a resonance state existing in the interaction of an upstream flexible filament and a downstream rigid body. Such resonance is a result of the synchronized vortex shedding behavior in the wake of the filament, as opposed to the natural vibration of the filament. In the resonance state, the flow-induced vibration of the filament is enhanced in terms of the flapping amplitude, but the drag on the filament is reduced despite the increase in the flapping amplitude. The resonant behavior in such a system is also evidenced by the soap film experiment with the different parameter setup from that in the numerical simulations. Both the experiment and the numerical simulation have shown that for the resonance to occur, the distance between the filament and the rigid body needs to be sufficiently small, and the Reynolds number needs to be high enough. The numerical investigation further shows that the filament length, mass ratio, and geometry of the rigid body have a significant effect on the flapping amplitude at resonance.

Since the resonance results from the vortex-vortex interaction in the flow, it would be interesting to investigate the

situation where the frequency of vortex shedding from the rigid body is a multiple of the filament flapping frequency. However, that study may require explorations in the parameter regime that is beyond what is considered here and therefore would be a topic for the future work.

The present results may provide a physical interpretation to the fact that some aquatic animals tend to swim in the bow wake of boats or stationary structures. Note that the present filament is not necessarily a realistic model of the swimming animals since the biological swimmers rely on their muscles to generate active body undulations. In the present study, the filament only responds to the flow passively [4]. However, the undulating animals could potentially take advantage of the flow-induced motion and the drag attenuation to reduce their own energy consumption. According to the present results, swimming either in the suppressed state or in the amplified state could benefit hydrodynamically the swimmers in the bow wake.

ACKNOWLEDGMENTS

We thank Professor X.-Z. Yin and Dr. S.-Y. Wang for their assistance in performing the experiments and the helpful discussions during the present work. F.-B. T. would like to acknowledge a support from China Scholarship Council during his stay at Vanderbilt University. X.-Y. L. is supported by the National Natural Science Foundation of China (Grant No. 10832010) and the Innovation Project of the Chinese Academy of Sciences (Grant No. KJCX2-YW-L05).

APPENDIX: THE LBM AND PIBM FOR FLAPPING FILAMENT WITH A FINITE MASS

1. Numerical method

The present solver combines a LBM and a PIBM for the coupled flow-filament dynamics. In the LBM, the kinetics of the fluid is governed by the discrete lattice Boltzmann equation of a single relaxation time model [24–26]. The multi-block LBM proposed in Ref. [27] is employed in the present work.

The fluid-solid boundary is handled by a modified version of the PIBM originally developed by Kim and Peskin [28]. In the PIBM, the no-slip boundary condition is achieved by adding a body force component \mathbf{b} to the momentum equation (1),

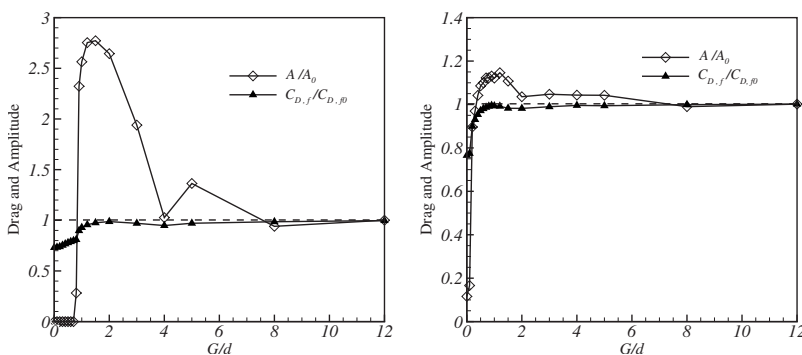


FIG. 13. (a) The amplitude and drag ratios of the filament with $S=0.5$, $Re=40$, and $L/d=2.5$. (b) The results for the filament in the bow wake of a rigid plate, where $Re=100$, $S=0.3$, and $L/d=2.5$.

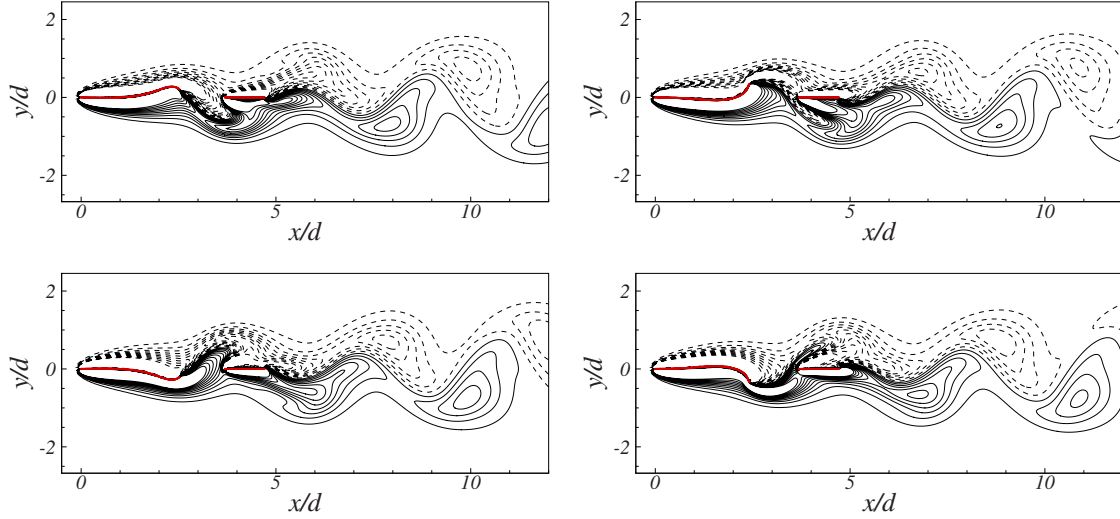


FIG. 14. (Color online) Instantaneous vorticity contours in a filament-plate system with $Re=100$, $S=0.3$, $L/d=2.5$, and $G/d=1.2$ (see the supplementary material [21] for an animation). The time interval is $1.1d/U$.

$$\mathbf{b}(\mathbf{x}, t) = - \int \mathbf{F}(s, t) \delta(\mathbf{x} - \mathbf{X}(s, t)) ds, \quad (\text{A1})$$

where $\mathbf{F}(s, t)$ is the Lagrangian force density representing the hydrodynamic force per unit area on the filament and is given by Eq. (2), $\delta(\mathbf{x} - \mathbf{X}(s, t))$ is the Dirac delta function, and \mathbf{X} is the position of a point on the filament. In the numerical method, the delta function is replaced with a smooth approximation adopted in Ref. [29].

The velocity of the filament is interpolated from the flow field onto the Lagrangian points discretizing the filament, and the position of those points is updated by explicitly integrating the velocity. A finite-difference method is used to calculate the stretching force and bending force terms in \mathbf{F} . To calculate the inertial force term, the penalty method used in Ref. [28] is adopted here to ensure the numerical stability. Specifically, the filament itself is assumed to be massless in the algorithm, but a ghost filament of linear density m_s is attached to the physical filament through a spring of stiffness K_v . The inertial term in Eq. (2) is thus replaced with the spring force. The details of the penalty method can be found in Ref. [28]. To deal with a nonelastic boundary such as the cylinder in the present problem, the Lagrangian force density \mathbf{F} is calculated based on the Navier-Stokes equation evaluated at the boundary [30]. Three problems are performed to validate the numerical algorithm used in the present work: (1) laminar flow past a stationary cylinder, (2) vortex-induced vibration of a cylinder, and (3) a single filament flapping in a uniform flow.

2. Laminar flow past a stationary cylinder

The two-dimensional laminar flow past a stationary cylinder is one of the canonical examples for testing the accuracy of a numerical method. The problem is solved here to assess the accuracy of the present PIBM-LBM solver. Simulations are run for $Re=20, 40, 60, 80, 100$, and 200 on a $40d \times 20d$ domain, where Re is the Reynolds number based on the free-stream velocity U and the diameter of the cylinder d .

The computational domain is discretized by a two-block Cartesian mesh. One is a uniform grid around the cylinder with the block size of $25d \times 6d$ and the resolution $\Delta x = \Delta y = 0.02d$. The other is a uniform grid covering the outer region with a coarser resolution, $\Delta x = \Delta y = 0.04d$. The average drag coefficient $C_D = F_D / (\frac{1}{2} \rho U^2 d)$ and the Strouhal number $St = fd/U$ are shown for various Re 's in Table I. Here, F_D is the mean drag force on the cylinder and f is the vortex shedding frequency. The results from several sources are listed in the table for comparison. It can be seen that our simulations are in very good agreement with the literature results for this stationary boundary problem.

3. Vortex-induced vibration of a cylinder

The vortex-induced vibration of a cylinder under subcritical Re is chosen to validate the present method for flow-structure interaction problems involving rigid bodies. The cylinder immersed in a uniform free-stream flow is mounted on two elastic supports and is free to vibrate in both the transverse and streamwise directions. The cylinder is subject to the hydrodynamic forces and also the spring forces. The mesh in the simulation is the same as that used in the previ-

TABLE I. Comparison of the mean drag coefficient C_D and Strouhal number St with previous data for the flow past a stationary cylinder.

Re	C_D/St (present)	C_D/St ^a [31]	C_D/St [32]	C_D/St [18]
20	2.156/-	2.09/-	2.04/-	2.23/-
40	1.620/-	1.58/-	1.54/-	1.66/-
60	1.494/0.138	1.44/0.143	-/-	-/-
80	1.444/0.155	1.40/0.158	1.40/0.150	-/-
100	1.428/0.166	1.39/0.169	1.39/0.160	1.42/0.171
200	1.438/0.198	1.39/0.204	-/-	1.42/0.202

^aThe $Re=200$ case in this column was simulated by using the same code from the authors.

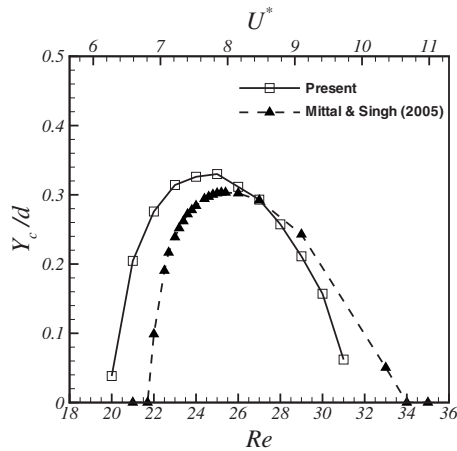


FIG. 15. The amplitude of the transverse oscillation in the vortex-induced cylinder vibration.

ous test. The nondimensional mass and the reduced natural frequency of the spring-cylinder system are $M=4m/(\pi\rho d^2)=4.73$ and $F_n=\frac{d}{2\pi U}\sqrt{\frac{k}{m}}$, where m is the mass of the cylinder and k is the stiffness of the supporting springs. The spring stiffness is specified in this test, so that $F_n=3.1875/Re$.

The amplitude of the vibration in the transverse direction, Y_c/d , as a function of Re , is shown in Fig. 15. The corresponding natural frequency, shown as $U^*=1/F_n=Re/3.1875$, is also provided (top axis). The result from Mittal and Singh [20] is plotted in the figure for comparison. Although there are some differences between our result and that of Mittal and Singh, the overall trends are consistent. The lower critical Re predicted by the present method is

between 19 and 20, and the upper critical Re is between 31 and 32. The critical Re of Mittal and Singh [20] is about 21.7 for the lower bound and 34 for the upper bound. In addition, the resonant vibration takes place at a slightly lower Re in our simulation, and the amplitude of the cylinder displacement is 8% higher than that of Mittal and Singh [20]. Considering that the critical Reynolds number for a stationary cylinder varies between 45.4 and 50 and the critical Strouhal number varies between 0.12 and 0.14 depending on the numerical method used by different authors [33–36], the present difference is acceptable.

4. Single filament flapping in a uniform flow

Here, we consider a lone filament flapping in a uniform flow. The mass ratio, defined by $S=m_s/\rho L$, where m_s is the linear density of the filament, ρ is the fluid density, and L is the length of the filament, is an important parameter in this problem. Both theoretical and numerical works [15,22,23] have shown that a low-mass filament in the uniform flow tends to have better stability than a high-mass filament. In addition, a massless filament is always stable even in the presence of large perturbations [23]. In our simulation, we also have the similar conclusions. For a quantitative comparison, we have computed the critical mass ratio S_c at which the filament transitions from a stable state to an unsteady flapping state at $Re=90$ (based on the filament length). In work of Connell and Yue [15], the critical mass ratio is $S_c=0.26$. In our simulations, S_c is between 0.22 and 0.28, which is consistent with the previous result. In addition, the flow pattern near S_c (not shown here) also agrees with those in Refs. [15,23].

-
- [1] M. M. Zdravkovich, *J. Fluids Eng.* **99**, 618 (1977).
 [2] C. R. Kyle, *Ergonomics* **22**, 387 (1979).
 [3] L. B. Jia and X. Z. Yin, *Phys. Rev. Lett.* **100**, 228104 (2008).
 [4] L. Ristroph and J. Zhang, *Phys. Rev. Lett.* **101**, 194502 (2008).
 [5] L. Zhu, *J. Fluid Mech.* **635**, 455 (2009).
 [6] J. C. Liao, D. N. Beal, G. V. Lauder, and M. S. Triantafyllou, *J. Exp. Biol.* **206**, 1059 (2003).
 [7] J. C. Liao, D. N. Beal, G. V. Lauder, and M. S. Triantafyllou, *Science* **302**, 1566 (2003).
 [8] J. C. Liao, *Philos. Trans. R. Soc. London, Ser. B* **362**, 1973 (2007).
 [9] P. F. Scholander, *Science* **129**, 1085 (1959).
 [10] A. A. Fejer, *Nature (London)* **188**, 700 (1960).
 [11] N. Bose and J. Lien, *Proc. R. Soc. London, Ser. B* **240**, 591 (1990).
 [12] D. N. Beal, F. S. Hover, M. S. Triantafyllou, J. C. Liao, and G. V. Lauder, *J. Fluid Mech.* **549**, 385 (2006).
 [13] J. D. Eldredge and D. Pisani, *J. Fluid Mech.* **607**, 279-288 (2008).
 [14] L. B. Jia and X. Z. Yin, *Phys. Fluids* **21**, 101704 (2009).
 [15] B. S. H. Connell and D. K. P. Yue, *J. Fluid Mech.* **581**, 33 (2007).
 [16] L. B. Jia, F. Li, X. Z. Yin, and X. Y. Yin, *J. Fluid Mech.* **581**, 199 (2007).
 [17] J. Zhang, S. Childress, A. Libchaber, and M. Shelley, *Nature (London)* **408**, 835 (2000).
 [18] S. Xu and Z. J. Wang, *J. Comput. Phys.* **216**, 454 (2006).
 [19] S. Alben, *J. Fluid Mech.* **641**, 489 (2009).
 [20] S. Mittal and S. Singh, *J. Fluid Mech.* **534**, 185 (2005).
 [21] See supplementary material at <http://link.aps.org/supplemental/10.1103/PhysRevE.82.026301> for the animations of the vorticity field at state S5 for filament-cylinder and filament-plate systems.
 [22] M. Shelley, N. Vandenbergh, and J. Zhang, *Phys. Rev. Lett.* **94**, 094302 (2005).
 [23] L. Zhu and C. S. Peskin, *J. Comput. Phys.* **179**, 452 (2002).
 [24] Z. L. Guo, C. G. Zheng, and B. C. Shi, *Phys. Rev. E* **65**, 046308 (2002).
 [25] S. Chen and G. D. Doolen, *Annu. Rev. Fluid Mech.* **30**, 329 (1998).
 [26] C. K. Aidun and J. R. Clausen, *Annu. Rev. Fluid Mech.* **42**, 439 (2010).
 [27] D. Yu, R. Mei, and W. Shyy, *Int. J. Numer. Methods Fluids* **39**, 99 (2002).
 [28] Y. Kim and C. S. Peskin, *Phys. Fluids* **19**, 053103 (2007).

- [29] X. Shi and N. Phan-Thien, *J. Comput. Phys.* **206**, 81 (2005).
- [30] E. M. Saiki and S. Biringen, *J. Comput. Phys.* **123**, 450 (1996).
- [31] T. Gao, Y. H. Tseng, and X. Y. Lu, *Int. J. Numer. Methods Fluids* **55**, 1189 (2007).
- [32] A. L. F. Lima E Silva, A. Silveira-Neto, and J. J. R. Damasceno, *J. Comput. Phys.* **189**, 351 (2003).
- [33] P. M. Gresho, S. T. Chan, R. L. Lee, and C. D. Upson, *Int. J. Numer. Methods Fluids* **4**, 619 (1984).
- [34] C. P. Jackson, *J. Fluid Mech.* **182**, 23 (1987).
- [35] M. Morzynski and F. Thiele, *Z. Angew. Math. Mech.* **71**, T424 (1991).
- [36] B. Kumar and S. Mittal, *Comput. Methods Appl. Mech. Eng.* **195**, 6046 (2006).